Check for updates

Terahertz hybrid optical-plasmonic modes: tunable resonant frequency, narrow linewidth, and strong local field enhancement

XINGGUO ZHENG,[1] JINGRUI WU,[1] JINHUA ZHANG,[1] ANQI YU,[1] YINGHAO YUAN,[1] XUGUANG GUO,[1,*] 🆔 AND YIMING ZHU[1,2,3]

[1]*Shanghai Key Lab of Modern Optical Systems, Terahertz Technology Innovation Research Institute, and Engineering Research Center of Optical Instrument and System, Ministry of Education, University of Shanghai for Science and Technology, Shanghai 200093, China*
[2]*Shanghai Institute of Intelligent Science and Technology, Tongji University, Shanghai 200092, China*
[3]*ymzhu@usst.edu.cn*
[*]*xgguo@usst.edu.cn*

Abstract: Hybrid optical-plasmonic modes have the characteristics of low loss and small mode volume, which will result in the strong localization and enhancement of electromagnetic field. Such advantages of hybrid optical-plasmonic mode are important for the enhancement of light-matter interactions. Here, terahertz (THz) hybrid modes of Fabry-Perot resonances (FPRs) and spoof surface plasmon polaritons (SSPPs) in the modified Otto scheme are investigated both in theoretical and experimental aspects. The device structure is composed of a metal grating silicon waveguide (MGSW) and a metal slit grating (MSG). The two components are vertically stacked with a variable air gap between them. The THz hybrid modes are originated from the far-field coupling of the FPRs and the SSPP supported by the air gap and the MSG, respectively. By changing the thickness of the air gap, the resonant frequency of the FPR-SSPP modes can be tuned in a frequency range of about 0.1 THz. An anti-crossing behavior between two reflection dips corresponding to the guided-mode resonance in the MGSW and the FPR-SSPP mode is observed, which leads to the narrowing of the reflection dips in the anti-crossing region. Numerical simulations show that at the resonant frequencies of FPR-SSPP mode, there is a huge volume-averaged electromagnetic energy enhancement of about 1600 times in the grooves of the MSG, which is around 8.7 times larger than that induced by the SSPP directly launched by free-space electromagnetic field. The hybrid FPR-SSPP modes can be used to construct THz sensors and detectors with high sensitivity.

1. Introduction

In 2004, Pendryet al. [1] theoretically predicted that on a textured perfect metal surface, low-frequency surface-propagating electromagnetic waves, named as spoof surface plasmon polaritons (Spoof SPPs, SSPPs), can be supported. Subsequently, Hibbins [2] and Williams [3] conducted experimental studies on such surface waves, and the results are consistent with the theoretical predictions [1]. The most remarkable characteristics of SPPs are small wavelength, slow group velocity, and strong localization on metal surfaces [4,5], which make SPPs have many potential applications [6–8]. However, at frequencies much lower than the plasma frequency of metals, for example, millimeter-wave and terahertz (THz) frequency bands, the above characteristics of SPPs (also called Sommerfeld surface waves at low frequency range) nearly disappear. SSPPs provide an important method to tightly bound low-frequency electromagnetic waves on dielectric-metal interfaces [9–12]. In comparison with traditional SPPs, SSPPs have the advantages of designable resonant frequency and low Joule loss, which make them attract widespread attention in recent years [13–16].

Due to the difference of dispersion relation, SPPs cannot be directly launched by electromagnetic waves from free space. For SSPPs, because there are two-dimensional (2D) or one-dimensional (1D) periodic subwavelength structures on metal surfaces [17], extra in-plane momentums are offered to the free-space electromagnetic waves and the SSPPs can be directly excited at some frequencies. However, in millimeter-wave and THz frequency regimes, for subwavelength 1D metal gratings, the efficiency of direct excitation of SSPPs is very low [18,19]. In general, the prism-based Otto configuration is used to launch SSPPs. In such an excitation scheme, there is a subwavelength air gap between the prism and the textured metal surface, and the SSPP is efficiently excited by the evanescent wave related to the total reflection of prism [20–26]. In order to ensure the phase matching of the evanescent wave and the SSPP, a prism with high refractive index is usually selected. Meanwhile, the Otto excitation efficiency of SSPP is very sensitive to the air gap between the prism and the textured metal surface, the frequency of electromagnetic radiation, and the incident angle, which limits the wide applications of the Otto excitation scheme. Therefore, it is important to realize a robust and efficient method to launch SSPPs.

In this paper, a modified Otto configuration is adopted to excite SSPPs, where the prism is replaced by a metal grating silicon waveguide (MGSW). In such modified Otto scheme, Fabry-Perot resonances (FPRs) supported by the air gap between the waveguide and a metal slit grating (MSG) are utilized to excite SSPPs, and hybrid FPR-SSPP modes are formed. Compared with the traditional Otto configuration [22,24], the modified excitation scheme has the advantages of easy control, far-field excitation, high efficiency, and tunable resonance frequency. In the Otto excitation scheme, the evanescent waves related to total reflection of prism result in the near-field excitation of SSPP. Therefore, the thickness of the air gap must be in the subwavelength range [27,28]. However, for the excitation of FPR-SSPP modes, there has no such a limitation, and the FPR-SSPP modes can be launched within a wide range of the air gap thickness. Due to the anti-crossing between the guided mode resonances (GMRs) in the MGSW excited by transverse magnetic (TM) electromagnetic wave and the FPR-SSPP modes, the excitation efficiency and the quality factor of the FPR-SSPP mode are enhanced. Furthermore, different from the fixed resonant frequency of SSPP in Otto configuration, the resonance frequency of FPR-SSPP can be tuned in the range of 0.65 THz-0.75 THz by changing the thickness of air gap. The first two branches of FPR-SSPP modes located in 0.65-0.75 THz range are formed with the air gap thicknesses in the ranges of 20-200 µm and 220-400 µm, respectively. The above advantages of hybrid FPR-SSPP mode are very important for constructing high-performance sensors.

The structural parameters of the modified Otto scheme are firstly estimated theoretically. Second, the reflection spectra, the resonant frequency and the field distribution of hybrid FPR-SSPP modes, and the local field enhancement are numerically simulated by using finite-difference time domain (FDTD) [29], and the structural parameters are optimized. Third, the modified Otto scheme is fabricated by using the standard planar semiconductor process. Finally, systematic experimental investigations are carried out by using a home-made THz time-domain spectrometer (THz-TDS). The experimental results are in good agreement with the theoretical and numerical simulation results. The resonant frequency of FPR-SSPP modes can be tuned from 0.65 THz to 0.75 THz by changing the thickness of air gap. The numerically calculated energy enhancement factor in the grooves of MSG is around 1600 (the maximum value: 1628) at the resonant frequencies of FPR-SSPP mode in a wide range of air gap. Moreover, near the anti-crossing region of GMR mode and FPR-SSPP mode, the linewidth of the reflection dip related to the FPR-SSPP mode is obviously reduced. Our investigations show that the hybrid FPR-SSPP modes have important potential applications in studying THz-matter interactions and improving the sensitivity of THz sensors and THz detectors [30,31]. The paper is organized as follows. In Section 2, the device structural parameters are designed and optimized, and the device fabrication process is briefly described. In Section 3, the theoretical and experimental results are presented and discussed. Finally, in Section 4, the main conclusions are drawn.

2. Structure design and sample preparation

The schematic diagram of the modified Otto scheme is shown in Fig. 1(a). The proposed device consists of a dielectric (high resistance silicon) slab with a 1D silver grating on it, and a subwavelength silver slit grating. The two components are vertically stacked with a variable air gap between them. The red wavy line represents the FPR generated in the air gap. The relative dielectric constant of silver grating on waveguide and the subwavelength silver slit gratings is described by the Drude model

$$\varepsilon_{\mathrm{m}} = 1 - \frac{\omega_{\mathrm{p}}^2}{\omega^2 + i\gamma_{\mathrm{p}}\omega} \tag{1}$$

where $\omega_{\mathrm{p}}=1.37\times10^{16}$ rad/s and $\gamma_{\mathrm{p}}=7.29\times10^{13}$ rad/s [32] are plasma frequency and scattering rate, respectively, ω is the angular frequency of the incident light, and i is the imaginary unit. TM THz electromagnetic waves are vertically incident to the combined structure, and the linear polarization direction is perpendicular to the 1D silver grating strips.
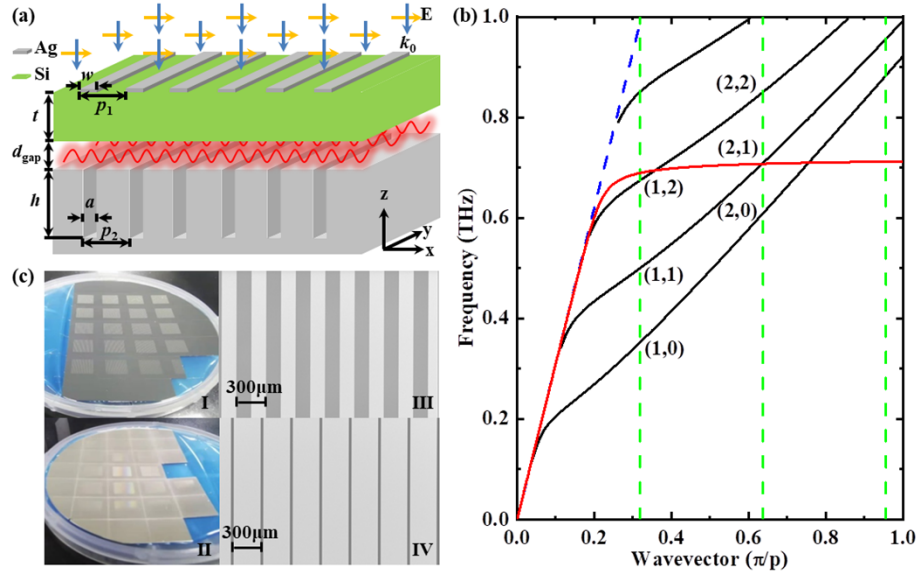

Fig. 1. (a) Schematic diagram of the modified Otto scheme (upper: MGSW, lower: MSG). The red wavy line represents the FPRs supported by the air gap. (b) The calculated dispersion relations of the first four-order GMR modes (solid black lines) supported by the MGSW, the SSPP (solid red line) supported by the MSG, and the free-space electromagnetic wave (blue dash line) for normally incident TM electromagnetic fields. The green dash lines represent the in-plane wavevectors provided by the 1D metal grating on the waveguide. The GMRs (cross-points) are labeled by (m, n) where m and n are the diffraction order of the metal grating on the Si waveguide and the guided mode order, respectively. The parameter values shown in (a) for calculating the dispersion relations are as follows: $p_1=300$ μm, $t=200$ μm, $p_2=300$ μm, $a=28$ μm, and $h=103$ μm. (c) The optical micrographs (I and II) and SEM images (III and IV) of MGSW (I and III) and MSG (II and IV) structures.

In the proposed modified Otto scheme, there are two SSPP excitation processes, the far-field FPR-SSPP coupling and the near-field coupling of GMR modes and FPR-SSPP modes. In the far-field FPR-SSPP coupling, due to the in-plane wavevector compensation of the periodic MSG structure, the SSPP can be excited by free-space electromagnetic waves. The reverse process, the SSPP coupling into free-space radiation (radiation loss) mediated by the MSG, severely limits

the free-space excitation efficiency of SSPP. In the proposed combined structure, by changing the thickness of air gap, the phase-match condition of FPR can be satisfied, which results in the formation of hybrid FPR-SSPP mode. Because the radiation loss is effectively suppressed, it is expected that the excitation efficiency of SSPP is increased substantially. In the near-field coupling of GMR modes and FPR-SSPP modes, GMRs are firstly excited by the vertically incident free-space TM electromagnetic waves in the silicon waveguide with the assistance of the metal grating on the silicon waveguide. When the air gap is in the subwavelength scale, the SSPP can be excited by the evanescent waves related to the GMRs.

To describe the near-field coupling, the dispersion relations of GMR and SSPP must be calculated. The dispersion relations of GMRs are firstly calculated. For simplicity, the coupling metal grating is not considered. The TM transcendental equation of the silicon waveguide is

$$\tan(\kappa t) = \frac{n_1^2 \kappa (n_3^2 \gamma + n_2^2 \delta)}{n_2^2 n_3^2 \kappa^2 - n_1^4 \gamma \delta} \tag{2}$$

and the parameters in Eq. (2) are

$$\kappa = (n_2^2 k_0^2 - \alpha^2)^{\frac{1}{2}} \tag{3}$$

$$\gamma = (\alpha^2 - n_2^2 k_0^2)^{\frac{1}{2}} \tag{4}$$

$$\delta = (\alpha^2 - n_3^2 k_0^2)^{\frac{1}{2}} \tag{5}$$

where t and n_1 are the thickness and the refractive constant of the slab dielectric waveguide, respectively, $n_2(n_3)$ is the refractive constant of above (below) environment of the waveguide, $k_0 = 2\pi f/c$ is the vacuum wavevector. The black solid lines in Fig. 1(b) are the dispersion relations for the first four order GMR modes. The green dash lines in Fig. 1(b) are the in-plane wavevector $k = 2\pi m/p_1$ provided by the metal grating, where m is the order of grating diffraction mode ($m = \pm1, \pm2, \pm3 \dots$). On the intersection points of the black solid lines and the green dash lines shown in Fig. 1(b), the phase-match condition for free-space TM electromagnetic wave excitation of GMRs is satisfied. As shown in Fig. 1(b) the GMRs are marked as (m, n) with n the GMR order.

Taking the metal loss into consideration, the dispersion relation of SSPP on a MSG can be expressed as [25,33]

$$k_{sspp} = \left(\varepsilon_d k_0^2 + \left(\frac{a\varepsilon_d}{p_2\varepsilon_g}\right)^2 k_g^2 \tan^2(k_g h)\right)^{\frac{1}{2}} \tag{6}$$

where

$$k_g = k_0 \sqrt{\varepsilon_d} \left(1 + \frac{l_s(i+1)}{a}\right)^{\frac{1}{2}} \tag{7}$$

is the wavevector inside the grooves, ε_g and ε_d denote the permittivity of the media inside the grooves and the top semi-infinite space of the structure, respectively; a and h are width and depth of groove, respectively; l_s denotes the skin depth of silver,

$$l_s = \left(k_0 Re\sqrt{-\varepsilon_m}\right)^{-1} \tag{8}$$

According to Eqs. (6)-(8), the dispersion relation of SSPP is calculated, and the resonant frequency of SSPP can be easily designed by adjusting the slit grating parameters, which is very useful for SSPP-based sensing applications. Actually, when the depth of groove is larger than the grating period, i.e., $h > Mp_2$ with M a positive integer, there exists high-order SSPP modes [25], but for the case of $h < p_2$, only the fundamental SSPP mode can be excited. The structural parameters of the MGSW (the thickness of silicon waveguide and the period of metal grating) and

the MSG (the width, height, and periodicity of MSG) are optimized by calculating the dispersion relations of GMRs and SSPP. The optimization criterion is that there are cross-points between the dispersion relations of GMRs and SSPP. The dispersion relation of SSPP with structural parameters of a=28 μm, p_2=300 μm, and h=103 μm, is shown in Fig. 1(b). It can be seen that at lower frequencies the wavevector of the SSPP is very close to that of the free-space light line and the dispersion relation curve deviates from the light line and approaches to the surface plasmon frequency of around 0.71 THz. This is a typical behavior of the dispersion relation of SPP in the optical frequencies, which indicates that a similar artificial surface bound state is achieved. As shown in Fig. 1(b), the second-order diffraction modes of the coupling metal grating on the silicon waveguide, the second-order GMR mode, and the SSPP mode intersect at a point, indicating that the SSPP can be efficiently excited by GMR via near-field coupling. Since the influence of the metal grating on the dielectric waveguide is neglected, inaccuracies on the calculation dispersion relations of GMRs should be introduced. Therefore, the commercial simulation package (Lumerical FDTD) [29] is used to conduct numerical simulations and to further optimize the structural parameters (thickness t and metal grating period p_1 of MGSW; period p_2, width a, and height h of MSG). Floquet periodic boundary conditions are used on the left and right sides of the computational domain, and two perfect match layers are added to absorb the transmission and reflection waves.

After optimizing the structural parameters, the two components of the combined structure are fabricated by using standard planar semiconductor fabrication process. For the MGSW structure, the period and the duty cycle of silver grating are p_1=300 μm and 50%, respectively; the thickness and the resistivity of silicon slab are t=200 μm and 10 kΩ·m, respectively. The experimental results show that the absorption of the high-resistivity (10 kΩ·m) silicon slab is negligible at frequencies lower than 1 THz. Three process steps are required to fabricate the MGSW structure: (i) A thick layer of AZ 9620 positive photoresist (5 μm) is spin coated on the silicon slab, and a periodic array of silver grating with an area of 15×15 mm^2 for each element is defined on the photoresist via conventional UV photolithography; (ii) a 600-nm-thick silver layer is then sputtered onto the photoresist; (iii) standard lift-off process is performed to obtain the silver grating strips. For the subwavelength MSG, the structural parameters of the rectangular groove are: width a=28 μm, period p_2=300 μm, and depth h=85 μm. Two fabrication steps are needed to obtain the MSG structure: (i) a rectangular groove array with an element area of 15×15 mm^2 is obtained through conventional UV photolithography and deep reactive ion etching on a 300-μm-thick silicon substrate; (ii) a 600-nm-thick silver layer is sputtered onto the processed silicon substrate. The optical micrographs and the detailed SEM images of gratings of the two structures are shown in Fig. 1(c).

3.   Results and discussion

In the following calculations, simulations, and experiments, only the case of normally incident TM electromagnetic waves with the electrical fields perpendicular to the metal strips on the MGSW is considered. The experimental reflection spectra of the combined structure are measured via a home-made fiber THz Time-Domain Spectroscopy system (THz–TDS) [34–36], and the resonant behaviors can be derived from the reflection spectra. The schematic diagram and the corresponding reflection THz path are shown in Fig. 2. The divergent THz pulses from the THz emitter (Fraunhofer, THz-P-Tx with a silicon hemispherical lens mounted) is collimated through the off-axis parabolic mirror 1 (DGMY-501105 with reflective focal length of 50.8 mm and caliber of 25.4 mm). A double-side polished high-resistance silicon wafer (235-μm thick) is inserted into the collimated THz beam path with a 45-degree azimuthal angle to the optical axis and a zero-degree polar angle to the vertical plane. Around 50% of the THz energy is transmitted through the silicon wafer, and the remaining 50% is reflected. The transmitted THz wave passes through a prismatic-shaped diaphragm and reaches samples or a high-reflectivity gold mirror.

The reflected THz wave from the samples/mirror passes through the diaphragm, is reflected by the silicon beam splitter, and is focused to the THz detector (Fraunhofer, THz-P-Rx mounted with a silicon hemispherical lens) by the off-axis parabolic mirror 2. Two home-made fiber femtosecond pulse lasers (Operating wavelength λ=1550 ± 20 nm, repetition frequency f_{rep}=100 MHz average power p=30-300 mW) are used as the pump and detection sources. The reflectance of gold mirror in THz range is very close to 1. Thus, a reflection spectrum of gold mirror can be used as the reference spectrum and the reflectance of sample can be obtained by dividing the reflection spectrum of sample by the reference spectrum.
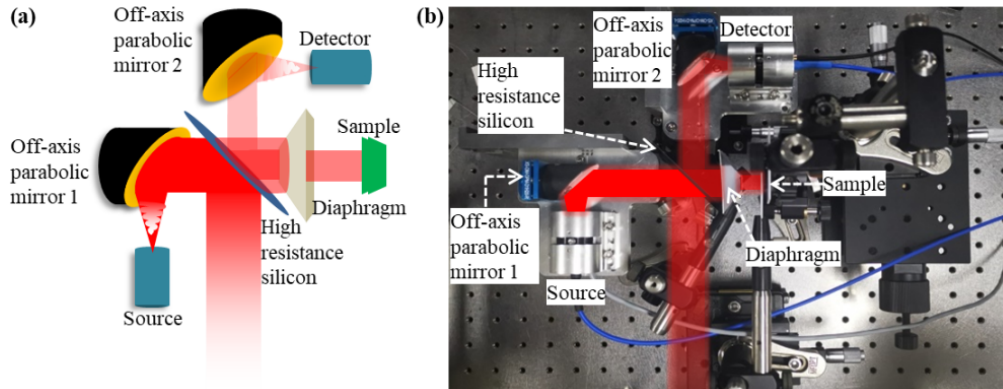

Fig. 2. (a) Schematic diagram of THz reflection spectrum measurement system, (b) experimental setup of THz emitter, detector, and optical path of the home-made fiber THz-TDS.

The reflection spectra related to the resonant behaviors of the two component structures are numerically simulated and measured separately. Before investigating the resonant behaviors of the vertically-stacked MGSW-MSG structure, the reflection spectra of the MGSW and MSG are individually simulated and measured. For the MGSW, in order to understand the spectral features due to the interference between the FPRs and GMRs, the reflection spectra of MGSW with different metal grating strip width are numerically investigated. A series of MGSW samples with w=30 μm, 60 μm, 90 μm, 120 μm, and 150 μm is fabricated and measured. The results are shown in Fig. 3(a). At the lowest duty cycle of 10%, it is clearly shown that there are two-types of reflection features for the MGSW structure. The broadband reflection features originate from the FPRs, and the sharp Fano reflection resonances are due to the interference of GMR modes with the background reflected waves. Without considering the influence of metal grating, the frequencies of FPRs are determined by $f = qc/2nt$ with q a positive integer, n=3.5 the refractive index of silicon. The derived frequencies of FPRs are 0.43 THz, 0.64 THz, and 0.86 THz for q=2, 3, and 4, respectively, which are in good agreement with the results shown in Fig. 3(a). All the simulated Fano reflection resonances (asymmetric and sharp reflection dips on the reflection spectra) can be identified by equaling the frequencies of these Fano reflection resonances and those of the (m, n) cross-points shown in Fig. 1(b). To further verify the origins of the Fano reflection resonances, the electric field distributions at the Fano resonant frequencies are given in Fig. S1 in the Supporting Information. To further verify the origins of the Fano reflection resonances, the electric field distributions are given in Fig. S1 in the Supporting Information. The experimental reflection spectra are in good agreement with the numerical ones. Due to the limitation of frequency resolution of the THz-TDS (300-ps-long sampling window, 3.3 GHz nominal frequency resolution), some Fano resonances with very sharp line shapes cannot be resolved. Such as the Fano reflection resonances at frequencies of 0.35 THz, 0.49 THz, 0.61 THz, 0.67 THz, and 0.71 THz for w=30 μm. With increasing the duty cycle of the coupling metal

grating, two additional effects play important roles. First, with increasing the width of metal grating strip, a non-negligible additional reflection phase at the upper surface of the MGSW is introduced, which results in the changes of FPR and GMR frequencies. Second, the radiation loss of GMR modes increases accompanied by the improvement of coupling efficiency, which leads to the broadening of the Fano resonances. It is worth to note that the linewidth and the resonant frequency of (2, 1) GMR mode at 0.71 THz designed to excited the SSPP mode have no distinct change. Figure 3(b) shows the numerical and experimental reflection spectra of the MSG. The reflection dips related to the SSPP mode are located at around 0.71 THz. There are two dips in the experimental reflection spectrum. The possible reasons maybe the poor silver layer quality in the narrow grooves, and the fluctuation of groove depth. The volume-averaged electric field distribution of $|E|^2$ in grooves at the frequency of lower reflection dip is shown in the insertion of Fig. 3(b). Numerical simulation shows that the volume-averaged electromagnetic energy in grooves is enhanced by around 187 times.
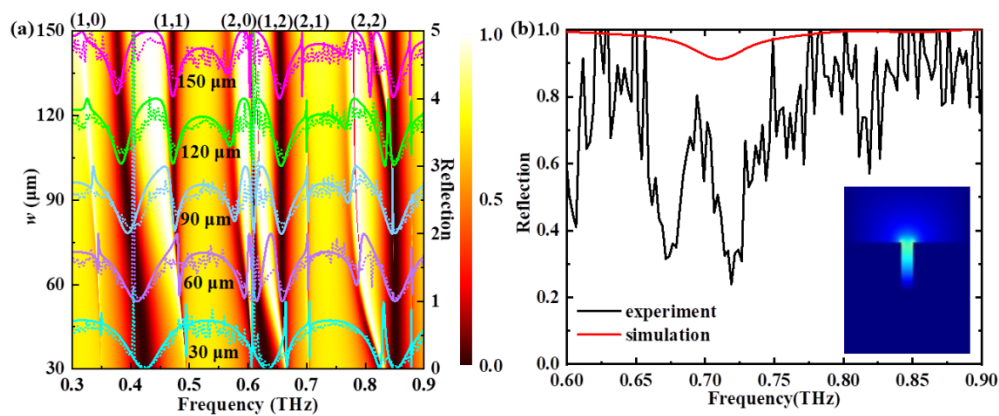

Fig. 3. (a) The pseudo-color contour of the numerical reflection spectra of the MGSW with period p_1=300 μm, thickness of Si slab t=200 μm and the metal strip width w as a sweeping parameter. The numerical and experimental reflection spectral curves with w increasing from 30 μm to150 μm (an increase step of 30 μm) are superimposed on the pseudo-color contour (solid and dotted lines represent the simulation and the experimental results, respectively). For clarity, the reflection spectra curves are vertically shifted. (b) The experimental (solid black lines) and numerically simulated (solid red lines) reflection spectra of the MSG.

Once the investigations on reflection spectra of the individual MGSW and MSG structures are completed, the resonant behaviors of the combined structure of vertically stacked MGSW and MSG are explored. The 50% duty cycle of coupling grating for the MGSW is selected due to its high coupling efficiency (Fig. S2 in Supporting Information). The pseudo-color contours of numerical and experimental reflection spectra with the thickness of air gap d_{gap} sweeping in the range of 0-500 μm are shown in Fig. 4(a) and (b), respectively. Because the material loss and the scattering loss are underestimated in simulations, the experimental linewidths of reflection dips are much larger than the simulated ones. Meanwhile, due to the finite frequency resolution (3.3 GHz) of THz-TDS, as shown in Fig. 4(b), some simulated reflection features with sharp linewidth in Fig. 4(a) cannot be well resolved. Except the above two differences, the main characteristics of the experimental reflection spectra with d_{gap} in the range of 0-500 μm are well corroborated by numerical simulations. In comparison with Fig. 3(a), there are two additional reflection dips in the frequency range of 0.68-0.78 THz in Fig. 4(b), which are relevant to the MSG structure. The main characteristics of the reflection dips are identified by the FDTD simulations (Fig. 4(a)). It is interesting to note that although the sharp reflection dip related to the (2, 1) GMR mode cannot be resolved experimentally, the anti-crossing points

are clearly observed in the experimental pseudo-color contour. There are minor discrepancies between the simulated and the experimental anti-crossing points (the vertical difference of d_{gap} is around 80 μm and the horizontal difference of frequency is 0.05 THz). Such differences are attributed to the poor quality of silver film in the sharp grooves of MSG. As shown in Fig. 1(b) and Fig. 3(b), the resonant frequency of SSPP is determined by the structural parameters and the environmental dielectric constant, which is very different from the results shown in Fig. 4 that the resonant frequency is dependent on d_{gap} and new branches appear periodically with further increasing d_{gap}. The electric field distributions at the reflection dips located at 0.65-0.75 THz in Fig. 4(c) show that the standing-wave pattern in the air gap and the strong field enhancement in the grooves of MSG appear simultaneously. Therefore, as shown in Figs. 4(a) and 4(b), we attribute the reflection dips in the frequency range of 0.65-0.75 THz (in the black dotted-line rectangles) to the formation of hybrid FPR-SSPP modes. The anti-crossing points in Fig. 4 is due to the coupling of (2, 1) GMR mode and the hybrid FPR-SSPP mode. At the same time, as shown Fig. 5, the bound state in the continuum (BIC) mode is formed near the anti-crossing point of GMR mode and hybrid FPR-SSPP mode, resulting in the narrowing of the reflection dip related to the hybrid FPR-SSPP mode. Such behaviors of air-gap-dependent resonant frequency of hybrid FPR-SSPP mode and linewidth narrowing near the anti-crossing point is important to constructing high-performance THz sensors.
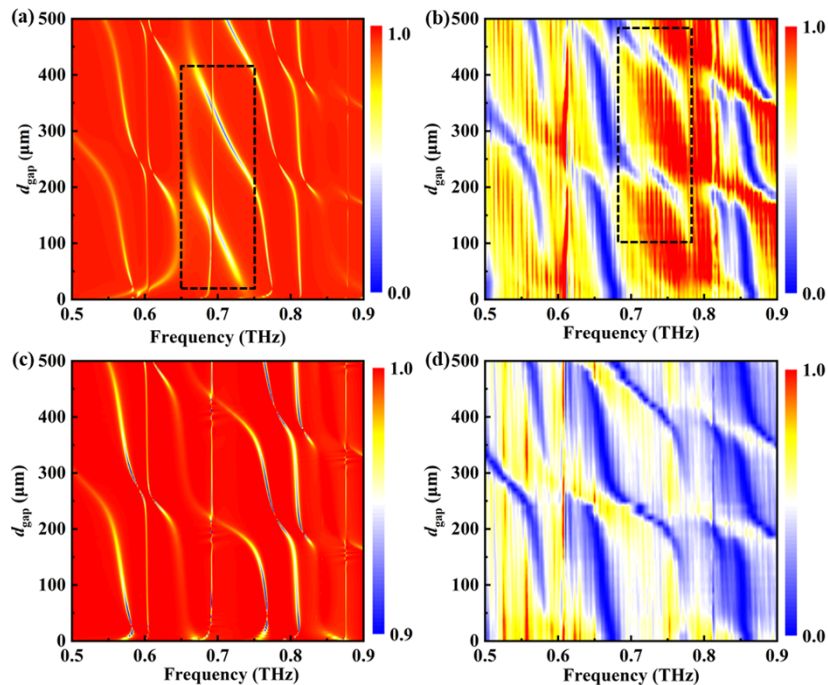

Fig. 4. Pseudo-color contours of simulation (a) and experimental (b) reflection spectra of the stacked MGSG-MSG structure with the thickness of air gap d_{gap} in the range of 0-500 μm. Pseudo-color contours of simulated (c) and experimental (d) reflection spectra of the vertically stacked structure of the MGSW and a planar gold mirror with an air gap in the range of 0-500 μm between them. The reflection dips in the frequency range of 0.65-0.75 THz in the black dotted-line rectangles shown in (a) and (b) originate from the formation of hybrid FPR-SSPP modes.

In order to further verify the origin of the reflection dips located in 0.65-0.75 THz shown in Fig. 4(a) and 4(b), the MSG is replaced by a planar gold mirror and the reflection spectra of
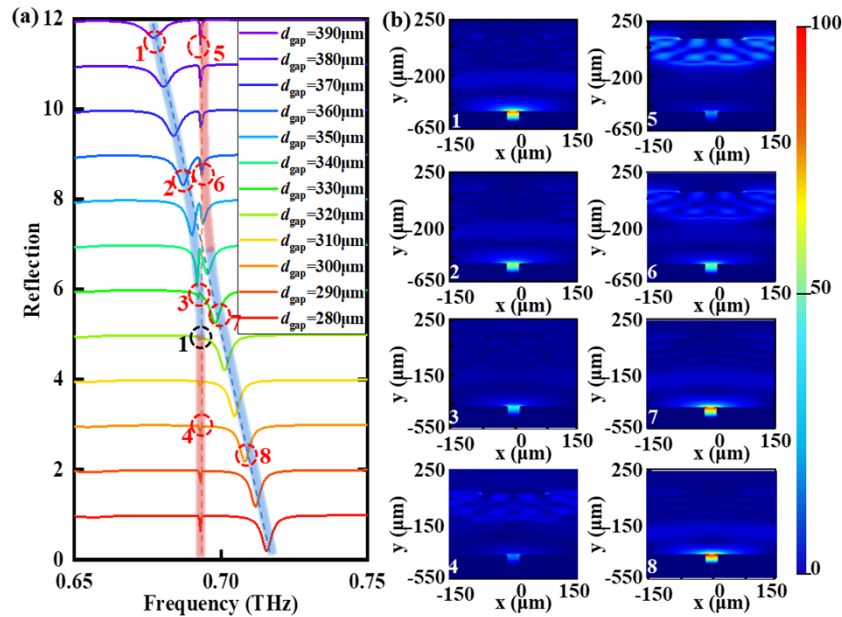
Fig. 5. (a) FDTD-simulated reflection spectra at different values of d_{gap} in the second anti-crossing branch in the dotted-line rectangle in Fig. 4, and (b) the electric field $|E|$ distributions at the reflection dip frequencies labeled by 1-8.

the new combined MGSW-gold-mirror structure are numerically simulated and measured with d_{gap} as a sweep parameter. The results are depicted in Fig. 4(c) and 4(d). Due to the ~100% reflectance of the gold mirror, and low material losses and Floquet periodic boundary conditions being set in the simulations, the calculated reflectance of all the reflection dips shown in Fig. 4(c) is larger than 90%. Except the discrepancy of reflectance and the experimentally unresolved narrow reflection dips, the numerical and experimental reflection behaviors shown in Fig. 4(c) and 4(d) are in good agreement with each other. In the frequency ranges of 0.5-0.65 THz and 0.78-0.9 THz, the simulated and experimental reflection spectra as a function of d_{gap} show very similar behaviors for the combined MGSW-MSG and MGSW-gold-mirror structures. However, in the frequency range of 0.65-0.75 THz, the reflection spectra are very different for the two combined structures, which indicates that the reflection dips at around 0.71 THz is related to the excitation of SSPP. In addition, for the same simulation parameters, the calculated reflectance of the reflection dip at around 0.71 THz for the MGSW-MSG structure is much lower than that for the MGSW-gold-mirror structure, which is a strong evidence of the excitation of the hybrid FPR-SSPP mode.

When the resonant frequencies of the hybrid FPR-SSPP mode gradually approach to the resonant frequency of the (2, 1)-order (the black dotted box in Fig. 4) GMR mode, the GMR-FPP-SSPP BIC is formed [37,38]. However, limited by the frequency resolution of our experimental system (THz-TDS), the reflection dips with narrow linewidths (high quality factor) cannot be well distinguished in experiment.

The reflection spectra at different values of d_{gap} in the second anti-crossing branch in Fig. 4(a) are plotted in Fig. 5(a), and the electric field $|E|$ distributions at the frequencies of reflection dips labeled by numbers 1-8 are plotted in Fig. 5(b). As shown in Fig. 5(a), when the resonant frequency of FPR-SSPP mode and the (2, 1)-order GMR mode approach to each other by changing the parameter d_{gap} continuously, an interference-induced avoided crossing of two reflection dips related to FPR-SSPP mode and GMR mode appears [39]. At d_{gap}=320 µm, the linewidth of

one of the reflection dips vanish exactly and its quality factor diverges (black dotted circle), which indicates the formation of a GMR-FPR-SSPP BIC [40]. Generally, the quality factor of a plasmonic mode is governed by the intrinsic metallic loss and the optical radiation loss [41]. At (near) the BIC points, the radiation into free space is inhibited (minimized); therefore, the quality factors of the hybrid GMR-SSPP modes around BICs are only metallic loss limited, which results in the linewidth narrowing of the reflection dip related to the FPR-SSPP mode [41]. From the electric field distributions 1-4 shown in Fig. 5(b), we find that the field localization position gradually shifts from the groove of the MSG to the slab silicon waveguide, which indicates that the reflection dip from 1 to 4 is gradually changed from the GMR-dominated to the FPR-SSPP-dominated. For the reflection dip from 5-8, the tendency is reverse.

As shown in Fig. 6(a), the MSG can be modeled as an effective anisotropic layer with the thickness being the same as the groove depth on a metal surface. Thus a combined FP resonant cavity of the air gap and the effective layer of MSG is formed. According to the effective medium theory [33], the equivalent dielectric constant of the effective medium of MSG for TM incident electromagnetic radiation is [42–46]

$$\varepsilon_{\text{eff}} = \frac{p_2}{(p_2 - a)/\varepsilon_m + p_2/\varepsilon_g} \tag{9}$$

The transfer matrix method (see Supporting Information) is used to calculate the reflection spectra of the equivalent model shown in the right of Fig. 6(a) and the vertically stacked structure of the Si waveguide and a planar gold mirror with the thickness of air gap d_{gap} in the range of 0-500 μm, respectively. The results are shown in Fig. 6(b) and 6(c). It can be seen that in the ranges of 0.5-0.65 THz and 0.85-0.9 THz, the reflection spectra of the two stacked structures show nearly the same behavior, but in the range of 0.65-0.85 THz, they are very different, which indicates that the SSPP can be described by the effective medium model qualitatively. Without considering the effects of GMRs, the calculated results using the transfer matrix method shown in Fig. 6(b) and 6(c) are qualitative accordance with those shown in Fig. 4(a) and 4(c).

All the results of FDTD simulations, the transfer-matrix calculations based on the effective medium model, and the measurements show that in the vertically stacked structure of MGSW and MSG, the reflection dips located in the frequency range of 0.65-0.75 THz are related to the excitation of the hybrid FPR-SSPP modes. With the assistance of the effective medium model presented in Fig. 6(a), the excitation mechanism of hybrid FPR-SSPP modes can be physically explained as follows. The air gap layer between the MGSW and MSG can be seen as a FP resonant cavity, and FPRs are excited when the total phase shift of a wave accumulates during one round trip in the resonator is a multiple of 2π. In the case of an air gap cavity, this leads to a resonance wavelength of [46]

$$\lambda = \frac{2n_0 d_{\text{gap}}}{(N + 1) - \frac{\Delta\varphi_{\text{refl}}}{\pi}} \tag{10}$$

where n_0 is the refractive index of the air gap cavity, N is an integer and $\Delta\varphi_{\text{refl}}$ is the phase shift upon reflection at a mirror which is π for a perfect metal. The behaviors of the resonant frequency shift and the periodic appearance of the hybrid FPR-SSPP mode with d_{gap} can be qualitatively explained by Eq. (10). If the planar gold mirror with high reflectance of the air gap cavity is replaced by the MSG, the phase shift upon reflection $\Delta\varphi_{\text{refl}}$ has to be replaced by the wavelength-dependent phase shift upon plasmon excitation $\Delta\varphi_{\text{exc}}(\lambda)$[46].

The influences of refractive index n of the upper dielectric layer on the hybrid FPR-SSPP modes are explored by using FDTD simulations. The numerical reflection spectra with respect to the upper dielectric layer refractive index n ranging from 1.0 to 3.5 are presented in Fig. 6(d). The reflectance of the reflection dip related to the hybrid FPR-SSPP mode increases with n changing from 1.0 to 3.5. The volume-averaged energy enhancement factor γ_E in a groove of MSG is
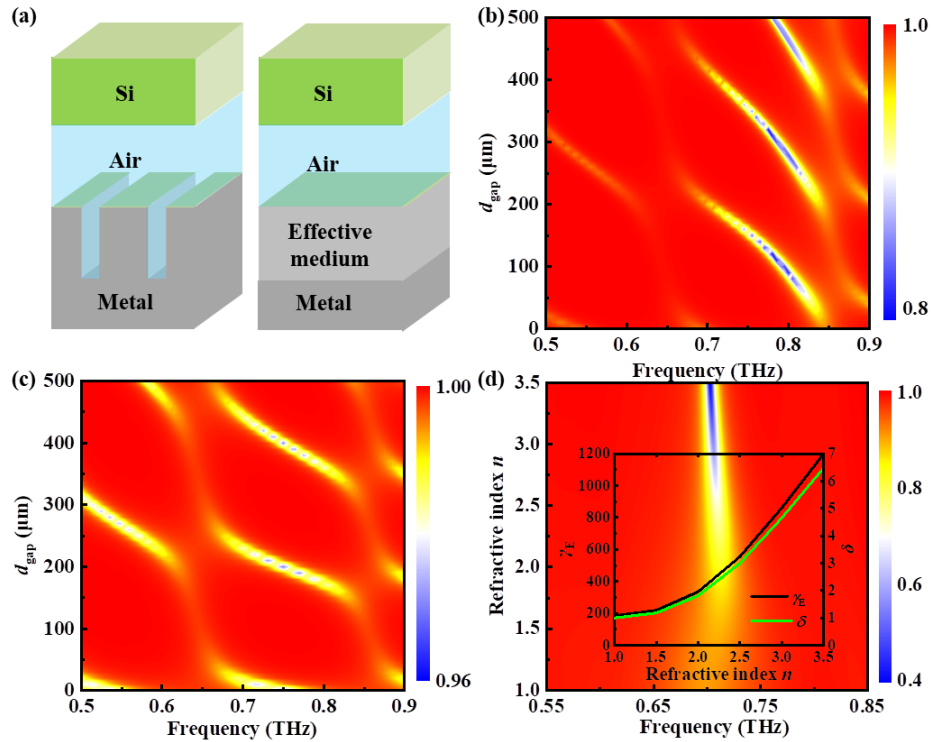
Fig. 6. (a) The vertically stacked structure of Si waveguide and MSG (left) and the corresponding equivalent model (right) where the MSG layer is replaced by an effective medium, (b) and (c) are the pseudo-color contours of reflection spectra of the equivalent model shown in the right of (a) and the vertically stacked structure of the Si waveguide and a planar gold mirror, and (d) is the numerical pseudo-color contour of reflection spectra of the structure shown in the right of (a) with $d_{\text{gap}}=100$ μm and the refractive index n of the upper waveguide ranging in 1 to 3.5. The inset in (d) shows the numerical results of the variation of volume-averaged electromagnetic energy enhancement factor γ_{E} in a groove of the MSG (black line) corresponds to the left axis and the relative enhancement factor δ (green line) with the refractive index n of the upper waveguide corresponds to the right axis.

defined as

$$\gamma_{\text{E}} = \frac{|E_{\text{groove}}|^2}{|E_{\text{inc}}|} \tag{11}$$

where E_{groove} is the volume-averaged field in the groove of MSG, and E_{inc} is the area-averaged incident field. The energy enhancement factor γ_{E} as a function of upper dielectric layer refractive index n is shown in the inset of Fig. 6(d) (black line). The value of γ_{E} super-linearly increases with respect to increasing refractive index n from 1.0 to 3.5, which indicates the high excitation efficiency of FPR-SSPP modes. In order to compare the energy enhancements in the groove of the MSG structure for the cases of FPR excitation and free-space excitation of SSPPs, the relative energy enhancement factor δ is defined as

$$\delta = \frac{\gamma_{\text{E}}}{\gamma_0} \tag{12}$$

where γ_0 is the volume-averaged electromagnetic energy enhancement factor in the groove of the MSG for the case of free-space excitation. It can be seen that as the refractive index of the upper

dielectric layer increases, the value of γ_E reaches up to around 1200 and the value of δ is 6.4 for n=3.5. According to Fresnel formula, the reflectance from the lower surface of the dielectric layer increases with the increase of n, which leads to the larger peak/valley ratio of FPR, the smaller radiation loss of SSPP, and the higher excitation efficiency of hybrid FPR-SSPP modes.

Finally, the effects of the air gap thickness d_{gap} on electric field distribution and energy enhancement factor in the air gap and in the groove of the MSG are explored. As shown in Fig. 7(a), the distributions of electric field $|E|$ labeled by I, II, III, and IV correspond to different values of d_{gap}=100 µm, 140 µm, 300 µm, and 340 µm and at the frequencies of the reflection dips related to FPR-SSPP mode, respectively. It can be seen that the electromagnetic energy can be effectively localized in the groove of the MSG when the hybrid FPR-SSPP mode is excited. When the resonant frequency of the hybrid FPR-SSPP mode gradually approaches to that of the (2, 1) GMR mode [40,47], an anti-crossing behavior occurs and a BIC is observed. In the anti-crossing region, the reflection dips have a higher quality factor [41], which is helpful for achieving a better resolution in sensing applications.
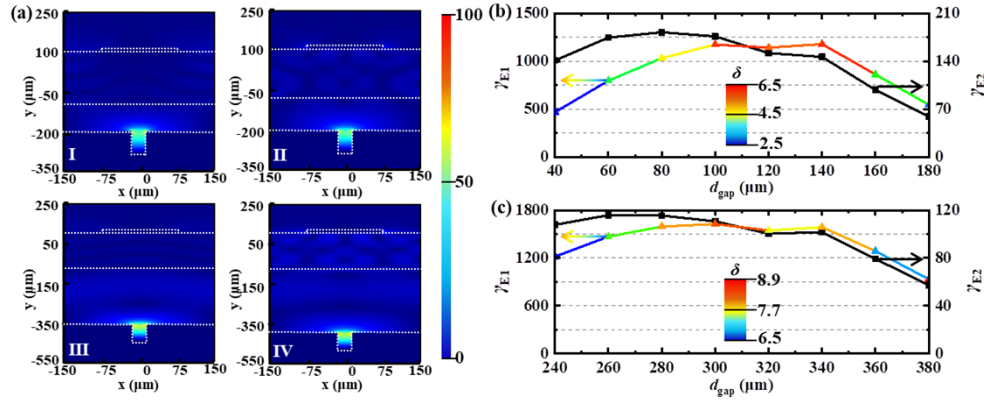

Fig. 7. (a) The electric field distributions of $|E|$ of the vertically stacked MGSW-MSG structure with the air gap thickness d_{gap}=100 µm (I), 140 µm (II), 300 µm (III), and 340 µm (IV); (b) and (c) the grove of MSG energy enhancement factors γ_E (colored-dot line) corresponding to the left axis and the air gap energy enhancement factors γ_{E2} (solid-dot black line) corresponding to the right axis at the resonant frequencies of the hybrid FPR-SSPP mode with the air gap thickness d_{gap} in the ranges of 40-180 µm and 240-380 µm, where the color bar indicates the value of relative energy enhancement factor δ.

The numerically simulated energy enhancement factors γ_{E1} (in the groove of the MSG) γ_{E2} (in the air gap) at the resonant frequencies of hybrid FPR-SSPP mode with the air gap thickness d_{gap} in the ranges of 40-180 µm and 240-380 µm are shown in Fig. 7(b) and 7(c), respectively. There are similar $\gamma_E - d_{gap}$ relations in the air gap and in the groove of the MSG. As shown in Fig. 7(b), the first peak value of γ_{E1} is 1175 at d_{gap}=100 µm and the second peak value of γ_{E1} is 1181 at d_{gap}=140 µm for hybrid GMR-SSPP mode with d_{gap} in the range of 40-180 µm. And for the GMR-FPR-SSPP mode with d_{gap} in the range of 240-380 µm, the first peak value of γ_{E1} is 1628 at d_{gap}=340 µm and the second peak value of γ_{E1} is 1587 at d_{gap}=340 µm shown in Fig. 7(c). The color bars in Fig. 7(b) and 7(c) represent the value of relative energy enhancement factor δ. It is worth to note that in a wide range of d_{gap}, a large value of relative energy enhancement factor δ is maintained.

4. Conclusion

In summary, a modified Otto configuration is developed to excite SSPP in THz regime. The modified Otto structure is composed of a MGSW and a MSG that are vertically stacked with

a thickness-tunable air gap between them. The resonant behaviors of the combined structure are numerically simulated, and then the structural parameters of the MGSW-MSG structure are designed and optimized by using theoretical calculations and numerical FDTD simulations. The designed MGSW-MSG structures are fabricated with the standard planar semiconductor fabrication process. The reflection spectra are systemically measured using a THz-TDS system. Based on an effective medium model, transfer-matrix calculations are performed to theoretically explain the resonant properties of the MGSW-MSG structure. The reflection spectral results of FDTD simulations, measurements, and the transfer-matrix calculations are in good agreements with each other. In the MGSW-MSG structure, optical-plasmonic hybrid FPR-SSPP modes are excited. In comparison with the SSPP mode excited by the traditional Otto configuration, the hybrid FPR-SSPP modes have several superior properties. The simulated resonant frequency of FPR-SSPP mode can be tuned from 0.65 THz to 0.75 THz by changing the thickness of air gap. A large volume-averaged energy enhancement factor of more than 1000 in the groove of the MSG can be maintained with the air gap thickness in broad ranges of 100-150 μm and 240-360 μm. The peak value of γ_E in the groove of the MSG can reach up to 1628, which is around 10 times larger than that for the free-space-excited SSPP mode. In the anti-crossing region of the (2, 1) GMR mode and the FPR-SSPP modes, spectral narrowing of the reflection dips can be observed. This work provides a useful method to realize optical-plasmonic hybrid modes in THz regime, which is important for constructing high performance THz sensors and detectors and for studying strong THz-matter interactions.

Disclosures. The authors declare no conflicts of interest.

Data availability. Data underlying the results presented in this paper are not publicly available at this time but may be obtained from the authors upon reasonable request.

Supplemental document. See Supplement 1 for supporting content.

References

1. J. B. Pendry, L. Martin-Moreno, and F. J. Garcia-Vidal, "Mimicking surface plasmons with structured surfaces," Science **305**(5685), 847–848 (2004).
2. A. P. Hibbins, B. R. Evans, and J. R. Sambles, "Experimental verification of designer surface plasmons," Science **308**(5722), 670–672 (2005).
3. C. R. Williams, S. R. Andrews, S. A. Maier, A. I. Fernández-Domínguez, L. Martín-Moreno, and F. J. García-Vidal, "Highly confined guiding of terahertz surface plasmon polaritons on structured metal surfaces," Nat. Photonics **2**(3), 175–179 (2008).
4. A. V. Zayats and I. I. Smolyaninov, "Near-field photonics: surface plasmon polaritons and localized surface plasmons," J. Opt. A: Pure Appl. Opt. **5**(4), S16–S50 (2003).
5. X. Guo, L. Xue, Z. Yang, M. Xu, Y. Zhu, D. Shao, Z. Fu, Z. Tan, C. Wang, J. Cao, and C. Zhang, "Strong terahertz absorption of monolayer graphene embedded into a microcavity," Nanomaterials **11**(2), 421 (2021).
6. A. V. Zayats, I. I. Smolyaninov, and A. A. Maradudin, "Nano-optics of surface plasmon polaritons," Phys. Rep. **408**(3-4), 131–314 (2005).
7. Y. Ren, X. Guo, G. Zhang, A. V. Balakin, A. P. Shkurinov, A. Yu, and Y. Zhu, "Excitation of graphene surface plasmons polaritons by guided-mode resonances with high efficiency," Opt. Express **28**(9), 13224–13233 (2020).
8. F. Ding, Y. Yang, R. A. Deshpande, and S. I. Bozhevolnyi, "A review of gap-surface plasmon metasurfaces: fundamentals and applications," Nat. photonics **7**(6), 1129–1156 (2018).
9. D. K. Gramotnev and S. I. Bozhevolnyi, "Plasmonics beyond the diffraction limit," Nat. photonics **4**(2), 83–91 (2010).
10. S. Hayashi and T. Okamoto, "Plasmonics: visit the past to know the future," J. of Phys. D **45**(43), 433001 (2012).
11. N. Liu, M. Mesch, T. Weiss, M. Hentschel, and H. Giessen, "Infrared perfect absorber and its application as plasmonic sensor," Nano Lett. **10**(7), 2342–2348 (2010).
12. S. Zhang, G. C. Li, Y. Chen, X. Zhu, S. D. Liu, D. Y. Lei, and H. Duan, "Pronounced Fano resonance in single gold split nanodisks with 15 nm split gaps for intensive second harmonic generation," ACS nano **10**(12), 11105–11114 (2016).
13. F. Garcia-Vidal, L. Martin-Moreno, and J. B. Pendry, "Surfaces with holes in them: new plasmonic metamaterials," J. Opt. A: Pure Appl. Opt. **7**(2), S97–S101 (2005).

14. M. Qiu, "Photonic band structures for surface waves on structured metal surfaces," Opt. Express **13**(19), 7583–7588 (2005).

15. L. Shen, X. Chen, and T. J. Yang, "Terahertz surface plasmon polaritons on periodically corrugated metal surfaces," Opt. Express **16**(5), 3326–3333 (2008).

16. B. Wang, L. Liu, and S. He, "Propagation loss of terahertz surface plasmon polaritons on a periodically structured Ag surface," J. Appl. Phys. **104**(10), 103531 (2008).

17. X. Guo, Y. Ren, G. Zhang, A. Yu, X. Chen, and Y. Zhu, "Theoretical Investigation on Microcavity Coupler for Terahertz Quantum-Well Infrared Photodetectors," IEEE Access **8**, 176149–176157 (2020).

18. B. Reinhard, K. M. Schmitt, V. Wollrab, J. Neu, R. Beigang, and M. Rahm, "Metamaterial near-field sensor for deep-subwavelength thickness measurements and sensitive refractometry in the terahertz frequency range," Appl. Phys. Lett. **100**(22), 221101 (2012).

19. B. Ng, J. Wu, S. M. Hanham, A. I. Fernández-Domínguez, N. Klein, Y. F. Liew, M. B. H. Breese, M. Hong, and S. A. Maier, "Spoof plasmon surfaces: a novel platform for THz sensing," Adv. Opt. Mater. **1**(8), 543–548 (2013).

20. A. Arbabi, A. Rohani, D. Saeedkia, and S. Safavi-Naeini, "A terahertz plasmonic metamaterial structure for near-field sensing applications," in, 33r (2008). d *International Conference on Infrared, Millimeter and Terahertz Waves*. IEEE. (2008), pp. 1–2.

21. Y. Huang, S. Zhong, T. Shi, Y. C. Shen, and D. Cui, "Trapping waves with tunable prism-coupling terahertz metasurfaces absorber," Opt. Express **27**(18), 25647–25655 (2019).

22. R. Zhao, G. Lu, H. Yin, J. Liang, D. Zeng, and H. Xiao, "Terahertz sensor study based on spoof surface plasmon polaritons," Int J Antennas Propag **2020**, 1 (2020).

23. T. Jiang, L. Shen, X. Zhang, and L. X. Ran, "High-order modes of spoof surface plasmon polaritons on periodically corrugated metal surfaces," Prog. Electromagn. Res. M **8**, 91–102 (2009).

24. X. Chen, H. Xiao, G. Lu, and R. Zhao, "Refractive index sensing based on terahertz spoof surface plasmon polariton structure," J Phys Conf Ser **1617** (1), 012008 (2020).

25. H. Yao and S. Zhong, "High-mode spoof SPP of periodic metal grooves for ultra-sensitive terahertz sensing," Opt. Express **22**(21), 25149–25160 (2014).

26. Y. Zhang, Z. Hong, and Z. Han, "Spoof plasmon resonance with 1D periodic grooves for terahertz refractive index sensing," Opt. Commun. **340**, 102–106 (2015).

27. H. Yao, S. Zhong, and W. Tu, "Performance analysis of higher mode spoof surface plasmon polariton for terahertz sensing," J. Appl. Phys. **117**(13), 133104 (2015).

28. Y. Huang, S. Zhong, T. Shi, Y. C. Shen, and D. Cui, "HR-Si prism coupled tightly confined spoof surface plasmon polaritons mode for terahertz sensing," Opt. Express **27**(23), 34067–34078 (2019).

29. The FDTD Solutions Trademark Software: http://www.lumerical.com.

30. Y. Peng, C. Shi, X. Wu, Y. Zhu, and S. Zhuang, "Terahertz imaging and spectroscopy in cancer diagnostics: a technical review," BME Frontiers. **2020**, 1–11 (2020).

31. Y. Peng, C. Shi, Y. Zhu, M. Gu, and S. Zhuang, "Terahertz spectroscopy in biomedical field: a review on signal-to-noise ratio improvement," PhotoniX. **1**(1), 12–18 (2020).

32. H. Shin, P. B. Catrysse, and S. Fan, "Effect of the plasmonic dispersion relation on the transmission properties of subwavelength cylindrical holes," Phys. Rev. B **72**(8), 085436 (2005).

33. A. Rusina, M. Durach, and M. I. Stockman, "Theory of spoof plasmons in real metals," Appl. Phys. A **100**(2), 375–378 (2010).

34. Z. Cheng, L. Chen, X. Zang, B. Cai, Y. Peng, and Y. Zhu, "Ultrathin dual-mode filtering characteristics of terahertz metamaterials with electrically unconnected and connected U-shaped resonators array," Opt. Commun. **342**, 20–25 (2015).

35. Z. Cheng, L. Chen, X. Zang, B. Cai, Y. Peng, and Y. Zhu, "Tunable plasmon-induced transparency effect based on self-asymmetric H-shaped resonators meta-atoms," J. Opt. **17**(3), 035103 (2015).

36. L. Chen, K. V. Truong, Z. Cheng, Z. Li, and Y. Zhu, "Characterization of photonic bands in metal photonic crystal slabs," Opt. Commun. **333**, 232–236 (2014).

37. A. Christ, S. G. Tikhodeev, N. A. Gippius, J. Kuhl, and H. Giessen, "Waveguide-plasmon polaritons: strong coupling of photonic and electronic resonances in a metallic photonic crystal slab," Phys. Rev. Lett. **91**(18), 183901 (2003).

38. S. G. Tikhodeev, N. A. Gippius, A. Christ, T. Zentgraf, J. Kuhl, and H. Giessen, "Waveguide-plasmon polaritons in photonic crystal slabs with metal nanowires," Phys. Status Solidi **2**(2), 795–800 (2005).

39. M. Meudt, C. Bogiadzi, K. Wrobel, and P. Görrn, "Hybrid photonic–plasmonic bound states in continuum for enhanced light manipulation," Adv. Opt. Mater. **8**(20), 2000898 (2020).

40. A. F. Sadreev, E. N. Bulgakov, and I. Rotter, "Bound states in the continuum in open quantum billiards with a variable shape," Phys. Rev. B **73**(23), 235342 (2006).

41. S. I. Azzam, V. M. Shalaev, A. Boltasseva, and A. V. Kildishev, "Formation of bound states in the continuum in hybrid plasmonic-photonic systems," Phys. Rev. Lett. **121**(25), 253901 (2018).

42. M. Born and E. Wolf, *Principles of optics: electromagnetic theory of propagation, interference and diffraction of light* (Cambridge University Press, 1999).

43. Y. Zhang, Y. Cui, W. Wang, K. H. Fung, T. Ji, Y. Hao, and F. Zhu, "Effective medium analysis of absorption enhancement in short-pitch metal grating incorporated organic solar cells," Opt. Express **24**(22), A1408–A1418 (2016).

44. D. L. Brundrett, E. N. Glytsis, and T. K. Gaylord, "Subwavelength transmission grating retarders for use at 10.6 μm," Appl. Opt. **35**(31), 6195–6202 (1996).

45. J. Ke, L. Yong-Qiang, H. Jun, Y. Chong-Min, W. Ying-Hui, and W. Hui-Na, "Middle-wave infrared and broadband polarization conversion based on metamaterial," *ACTA PHYS SIN-CH ED* 66(13), (2017).

46. R. Ameling and H. Giessen, "Microcavity plasmonics: strong coupling of photonic cavities and plasmons," Laser Photonics Rev. **7**(2), 141–169 (2013).

47. C. W. Hsu, B. Zhen, A. D. Stone, J. D. Joannopoulos, and M. Soljačić, "Bound states in the continuum," Nat. Rev. Mater. **1**(9), 16048–13 (2016).